Journal of Magnetic Resonance Open 21 (2024) 100175

Contents lists available at ScienceDirect

Journal of Magnetic Resonance Open

journal homepage: www.sciencedirect.com/journal/journal-of-magnetic-resonance-open

A standardized MRI phantom for dissolved phase ^{129}Xe MRI

Max Filkins [a,b], Arthur Harrison [a,c,d], Guilhem J. Collier [e], Graham Norquay [e,f], Jim M. Wild [e,f], Sean P. Rigby [b], Galina E. Pavlovskaya [a,c,d], Thomas Meersmann [a,c,d,g,*]

[a] Sir Peter Mansfield Imaging Centre, University of Nottingham, NG7 2RD, UK
[b] Department of Chemical and Environmental Engineering, University of Nottingham, NG7 2RD, UK
[c] Translational Medical Sciences, School of Medicine, University of Nottingham, Nottingham, NG7 2UH, UK
[d] NIHR Nottingham Biomedical Research Centre, Nottingham University Hospitals, NHS Trust, Queen's Medical Centre, Derby Road, Nottingham NG7 2UH, UK
[e] POLARIS, Division of Clinical Medicine, School of Medicine & Population Health, University of Sheffield, Sheffield, UK
[f] Insigneo Institute, University of Sheffield, UK
[g] Centre of Life Sciences and Health Care, University of Nottingham, Ningbo, China

ARTICLE INFO

Keywords:
Hyperpolarization
Hyperpolarized 129Xe
Pulmonary MRI
Dissolved phase xenon-129 phantom
EXSY NMR
Red blood cell chemical shift standard
Tissue and plasma gas uptake

ABSTRACT

Pulmonary MRI of hyperpolarized xenon-129 (hp^{129}Xe) dissolved in the lung parenchyma and vascular phase is gaining increasing attention for clinical assessment of gas exchange in multiple diseases. These conditions can involve thickening of barrier tissues due to fibrotic scarring or reduced capillary blood flow leading to diminished gas-blood exchange hence, the ratios between hp^{129}Xe signals arising from the lung membrane (M), the red blood cells (RBC), and the gas phase hold significant diagnostic value. However, comparing hp^{129}Xe signal ratios quantitatively across different studies may pose challenges due to varied experimental conditions and opted pulse sequence protocols.

A solution to this problem arises from materials science applications of hp^{129}Xe where xenon dissolved in porous materials or polymers can display chemical shifts similar to the M and RBC shift in lungs. This work explored the generation of MR spectral profiles with respect to chemical shift and signal intensity ratios that closely resemble spectral profiles observed in human lungs in health and disease. At ambient temperatures, reticulated open cell polyurethane foam treated with olive oil as a fatty phase produced dissolved phase ^{129}Xe chemical shifts of 215 ppm and 196 ppm, respectively, that emulate typical RBC and M signals. The uptake kinetics into the non-toxic materials was sufficiently similar to pulmonary signal uptake to enable hp^{129}Xe MRI with dissolved phase ratios that closely resembled clinical data.

A phantom assembly was devised to allow for gas handling protocols that matched clinical protocols. The current iteration of the developed phantom enables rapid testing of basic experimental protocols and can be used for training purposes without regulatory approval and governance. Furthermore, the introduced concept shows a pathway for the development of a quantitative universal phantom standard for dissolved phase pulmonary hp^{129}Xe MRI. A robust phantom standard will require materials with longer shelf lifetime than the oil-foam system used in this study and would benefit from a hierarchical porous network with more defined microstructure similar to that found in lungs.

1. Introduction

As an emerging technology, hyperpolarized xenon-129 (hp^{129}Xe) magnetic resonance imaging (MRI) enables significant advancement over current pulmonary diagnostics and prognostics with a high potential for efficacy monitoring in stratified medicine, drug development and preventive care [1–7]. Beyond research applications, the technology has already received clinical approval to a varying degree in at least three countries (UK in 2016; PR China and USA in 2022). Similar to hyperpolarized helium-3 (hp^{3}He), inhaled hp^{129}Xe can be used for functional lung MRI of ventilation [1,8,9] and diffusion-weighted contrast enables insights into lung microstructure [1,8]. Furthermore, hp^{129}Xe has an additional and unique property of distinguishable, characteristic MR signals arising from xenon dissolved in tissue and blood. The hp^{129}Xe MR signal from pure xenon gas, approximated to zero density, often serves as the shift standard for xenon and is referenced to 0 ppm. The ^{129}Xe signal shift in (pure) gaseous as a function of xenon density is only about +0.55ppm/amagat [10,11] which

* Corresponding author.

https://doi.org/10.1016/j.jmro.2024.100175

Available online 9 November 2024

approximately translates to +0.55ppm/bar in (pure) gaseous xenon at ambient pressure and below. This small dependence of the ^{129}Xe shift on the gas pressure is further reduced due to dilution of the hp^{129}Xe with residual air in the lung. Due to the lower spectral resolution of clinical (and pre-clinical) MRI scanners compared to high-resolution NMR spectrometers, it is therefore usually adequate to designate the ^{129}Xe signal obtained from the pulmonary gas phase as the 0 ppm reference signal. However, a slightly stronger shift may be caused by the magnetic susceptibility of tissue in the lung. Driehuys and co-workers have recently reported two distinct gaseous ^{129}Xe resonances in rodent (mice) lungs arising from conducting airways with a range of -0.6 ± 0.2 to $+1.3 \pm 0.3$ ppm and the alveolar region exhibiting a relatively stable value of -2.2 ± 0.1 ppm [12]. This susceptibility shift is still fairly small compared to dissolved phase chemical shifts. Future refinement of the phantom materials can (and should) take susceptibility effects for gas and dissolved phase signals into account, in particular once data from human subjects becomes available.

In the human lung, three signals are observed after hp^{129}Xe inhalation: (1) the pulmonary gas phase signal, here referenced to 0 ppm; (2) the signal arising from xenon dissolved in the tissue or membrane (M) at around 197 ppm [13] (note that 'tissue and plasma' (TP) is often used in literature instead of M); and (3) the signal arising from ^{129}Xe within the red blood cells (RBC). The RBC signal exhibits a range of shifts between 218 - 219 ppm at typical pulmonary blood oxygenation levels between 0.80 – 0.87 [5,14,15]. The possible RBC chemical shift range has been explored previously in vitro with the maximum value of 222 ppm observed in 100 % oxygenated blood samples that quickly drops by 4–5 ppm when the oxygenation is lowered to 80 %. Any further reduction only causes minor changes with a minimum value of 216 ppm at 0 % blood oxygenation [5,13–15]. Pulmonary diseases may lead to reduced oxygenation levels and hence lower chemical shift values as demonstrated, for example, in a rat model of bronchopulmonary dysplasia that led to an about 0.55 ppm reduced value [16] (i.e. from about 212 ppm as the RBC chemical shift values are species dependent).

Dissolved phase xenon only amounts to about 1 – 2 % of the amount of inhaled xenon in the alveolar region. However, a rapid diffusive xenon exchange between the alveolar gas phase and the dissolved phases can be probed through various protocols. Early work explored the saturation through selective radiation of the M and RBC signals that, via gas exchange, leads to a reduction in the observed gas phase signal intensity in xenon polarization transfer contrast (XTC) protocols [17,18]. Alternatively, the recovery kinetics of the saturated (or in some experiments inverted) magnetization of M and RBC dissolved hp^{129}Xe can be explored through chemical shift saturation recovery (CSSR) experiments [19–23,24]. Distinction between M and RBC phases can be made, for example, through a variant of the Dixon technique as demonstrated in early pre-clinical MRI [25]. Not limited to the Dixon method, chemical shift selective protocols that excite the M or RBC dissolved phase hp^{129}Xe allow for the amplification of these signals through fast averaging because the magnetization is recovered through exchange with the (undisturbed) gas phase hp^{129}Xe [26,27]. The enhancement of the RBC signal hinges on the exchange dynamics among the gas, tissue, and vascular phases. Consequently, monitoring the exchange of hp^{129}Xe through the parenchyma becomes viable and can be leveraged for functional pulmonary MRI. For instance, in interstitial diseases, the RBC signal might decrease due to fibrotic scarring, which thickens the barrier tissue separating the air and vascular phases. Conversely, the M signal could increase owing to the rise in barrier tissue volume. The hp^{129}Xe signal intensity, referenced to the intensity of either the gas phase or the M signal, i.e. RBC/gas or RBC/M, therefore serves as a biomarker of reduced oxygen transfer in affected regions of the lung [5]. Dissolved phase hp^{129}Xe MRI and magnetic resonance spectroscopy (MRS) are still at an earlier stage of development compared to hp^{129}Xe ventilation and pulmonary MRI utilizing hp^{129}Xe apparent diffusion contrast (ADC). Nevertheless, the spatially unresolved RBC/M ratio observed through hp^{129}Xe MRS has been shown to provide a sensitive lung global metrics of significantly reduced gas exchange in patients with idiopathic pulmonary fibrosis (IPF) compared to healthy volunteers ($p < 0.0002$), a metrics that strongly correlated with the pulmonary transfer factor for carbon monoxide (TL_{CO}) [28]. A statistically significant difference in alveolar septal thickness between healthy volunteers and patients with IPF and scleroderma (SSc) was found in a time-resolved hp^{129}Xe MRS pilot study, although no statistically significant distinction could be drawn between the patient groups [29]. Recent advances allowed for the detection of disease progression in longitudinal studies of IPF through hp^{129}Xe MRS with improved sensitivity to 12 month change in patients with IPF ($p = 0.001$) compared to current clinical metrics such as FVC ($p = 0.048$) and TL_{CO} ($p = 0.881$) [30]

Beyond the hp^{129}Xe MRS lung global metrics, gas exchange hp^{129}Xe MRI allows for the visualization of regional gas exchange impairment in IPF with strong correlation to TL_{CO} metrics [31–33]. Reduced RBC/gas and RBC/M ratios are mainly observed in peripheral and basal regions of the IPF affected lungs [34] This observation corresponds qualitatively with fibrosis observed via CT, however only a weak correlation with CT fibrosis scoring has been found. Gas exchange hp^{129}Xe MRI displays a high sensitivity to longitudinal IPF disease progression [30,35]. Hp^{129}Xe MRI and MRS can be utilised to differentiate between cardiopulmonary function impairment in COPD, IPF, left heart failure (LHF) and pulmonary arterial hypertension (PAH) [36]. In the wake of the COVID pandemic, a reduced gas-blood exchange was demonstrated through CSSR MRS in hospital discharged COVID patients [23]. The long-term persistence of this pathophysiology was demonstrated in a longitudinal, multi-centre study using dissolved phase hp ^{129}Xe MRI in patients after their discharge from the hospital intensive care units (ICUs) [37–39].

The growing interest in hp^{129}Xe dissolved phase pulmonary MRI makes a common standard desirable as different experimental parameters and protocols, such as: RF pulse flip angles [40], magnetic field strength B_0, and pulse sequence timing can all affect the observed signal ratios. For example, the RBC/gas and M/gas ratios don't reflect the true ratio of hp^{129}Xe atoms in the various phases as only a small flip angle is applied to the gas phase to preserve its polarization. Any changes in the hp^{129}Xe gas phase flip angle will therefore directly affect the observed RBC/gas and M/gas ratios. The proposed multicentre studies with dissolved phase hp^{129}Xe [41] suggest likely utility and significance for a common standard.

Obtaining data from healthy volunteers presents challenges for standardization due to inherent variability and age/gender related dependencies [42,43]. Additionally, there are delays and heightened costs associated with the necessary regulatory procedures, further complicating the process. Similar considerations apply to the training of personnel and the establishment of new sites for hp^{129}Xe dissolved phase MRI. In this work, building on the extensive field of ^{129}Xe NMR research and applications in material sciences [4,44], we test a first prototype of a hp^{129}Xe dissolved phase phantom of human lungs. The intended applications for the phantom standard require the usage of hp^{129}Xe rather than high pressure thermally polarized ^{129}Xe as was reported for a previous (gas phase only) phantom that has very different, complementary purposes and merits [45]. However, usage of hp^{129}Xe is essential for testing and calibrating of specialized dissolved phase MRI protocols because the signal intensity in the dissolved phase is too low for thermally polarized ^{129}Xe, even at elevated pressures. Most significantly, probing the gas exchange dynamics specifically requires hp^{129}Xe because thermally polarized ^{129}Xe MRI would be based on relaxation recovery rather than gas exchange, leading to very different signal intensity ratios. The phantom development also seeks to significantly streamline pulmonary MRI training and protocol testing with hp^{129}Xe. As an ultimate goal, this work intends to provide a route to a future universal standard test object.

To advance a dissolved phase standard, the following design conditions were targeted:

A. The standard must contain materials with a dissolved phase ^{129}Xe spectral signature that closely resembles the ^{129}Xe chemical shifts for RBC and M in human lungs.
B. The observed ^{129}Xe signal intensity ratios (i.e. RBC/M, RBC/gas, and M/gas) should be similar to those found in human lungs, well defined, and reliably reproducible.
C. The kinetics of the hp^{129}Xe uptake should be similar to that in human lungs, well defined, and reliably reproducible. Variation in experimental parameters should lead to predictable changes in the ^{129}Xe signal intensity ratios.
D. In future iterations, it might become necessary to create standards that replicate specific pulmonary conditions and in vivo temperature/pressures. The proposed standard framework should accommodate such advancements and developments.
E. The operational procedure for the standardized phantom should closely resemble clinical protocols where the hp^{129}Xe is inhaled by the patient from a Tedlar™ bag.
F. The materials employed must be safe for handling, preferably non-toxic, and should exhibit minimal vapor pressure at room temperature.
G. The phantom should have a reasonable shelf lifetime of at least 18 months.

The reported developmental work of a phantom standard was focused on emulating the hp^{129}Xe signals arising from the RBC and M phases in human lungs in health and disease but the devised concept can be extended to other human organs such as the brain [46] and to animal models of disease [16,47].

2. Methods

Experimental hardware for 9.4T NMR spectroscopy. All non-imaging nuclear magnetic resonance (NMR) spectroscopic work was performed using a 9.4 Tesla Bruker Avance III NMR spectrometer with a vertical 89 mm diameter, clear-bore, superconducting magnet and a custom-built NMR probe resonating at the ^{129}Xe frequency of 110.7 MHz. A home-built hyperpolarizer, with a 65 W diode array laser (Shark 65 W narrow linewidth laser system by OptiGrate Corp., USA) tuned to 794.7 nm, similar to a previously described version [48] was used for spin exchange optical pumping (SEOP). SEOP of a 5 %:95 % Xe:N_2 gas mixture at near ambient pressure of 110 kPa (1.1 bar) produced a continuous flow of hp^{129}Xe with a spin polarization $P = 12$ % available to (and measure by) the NMR experiment. Xenon gas with 26.4 % ^{129}Xe natural abundance isotope distribution (BOC limited, UK) was used in this work exclusively. For the characterization of the polymer foams, NMR detection took place as depicted in Fig. 1A under continuous flow at near ambient pressure of 110 kPa and temperature of 293 K, with the exceptions of stopped-flow (or batch-mode) measurement using 100 % xenon gas after cryogenic separation and for measurements in bulk oil phase (see descriptions below). Note however, 'batch-mode' only refers to the NMR measurments as in both cases the SEOP process took place under continuous flow conditions. A steady flow rate of 1.8 ± 0.05 ml/s was applied for all continuous flow experiments.

Reticulated polyurethane foams and oils used. Consumer grade extra virgin olive oil was used as a safe, non-toxic, low vapour pressure component, except for one experiment conducted with vacuum pump oil (Edwards, Ultragrade Performance Vacuum Oil 19). The various foams were obtained from Zouch Converters Ltd (Nottingham, UK) as 10 mm thick, DIN A4 sized (210 mm x 297 mm) foam sheets. The reticulated polyurethane foams by ZOUCH (ZR), with various open pore sizes described by 'pore per inch' (PPI) and their colour are: ZR20-black, ZR20H-green, ZR30H-beige, ZR45-black, ZR45H-blue, ZR60-black, ZR85H-beige, ZR90-black. Note these open pore foams are typically used for filters. Small, approximately 20 mm x 15 mm x 10 mm foam samples were cut from the sheets and used either dry or impregnated with the olive oil at various mass percentages where 100 % refers to a 1:1 mass ratio of oil:foam (m_{oil}/m_{foam}). The oil mass was measured with a high precision balance (Satorius, MC1) after an approximate quantity of oil was added to a cut foam sample and then manually massaged into the foam using standard latex gloves.

Hp^{129}Xe spectra of the foam and the foam – oil system. Hp^{129}Xe spectra of foams were obtained under continuous flow conditions as described previously [49] with the sample container depicted in Fig. 1A. A 90° excitation pulse (68 us duration) was used, followed by a recycle delay of 5 s for 64 averaged scans to obtain good SNR ratios for the dissolved phase. One experiment was conducted with 100 % hpXe (natural abundance ^{129}Xe) obtained through cryogenic separation from the SEOP mixture followed by transfer through pressure equalisation into the pre-evacuated sample chamber [50]. The spectrum was detected in a single scan, approximately 5 s after gas transfer at ambient pressure and 293 K.

One Dimensional Exchange Spectroscopy (1D-EXSY). For the

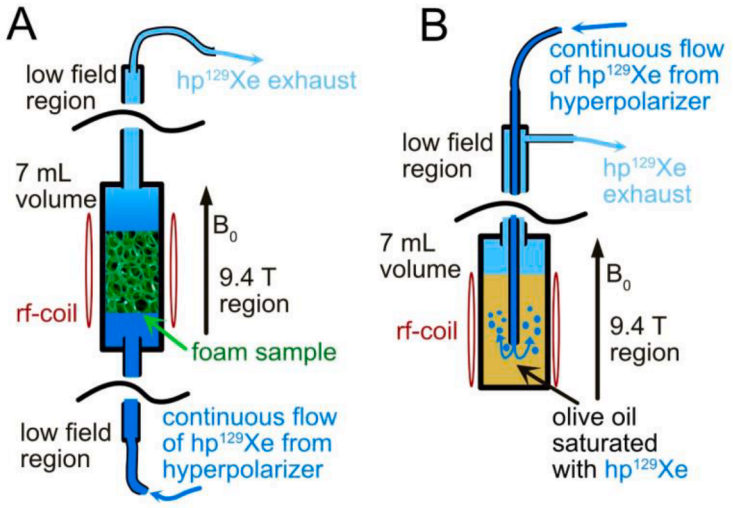

Fig. 1. Sketch of the continuous flow experimental setups used for hp^{129}Xe NMR measurements in an upright (vertical bore) 9.4 Tesla superconducting magnet. A custom-built probe with 15 mm clear-bore inner diameter (ID) to accommodate the sample holder and gas transfer lines was used and the coil region extends over 25 mm in the z-direction. **(A)** PFA tubes (1/8 inch outer diameter (OD) with approximately 1/16 inch ID facilitated a continuous flow of hp^{129}Xe gas into (and out of) the 50 mm long, 13 mm ID, acrylic sample cell used to study a series of foam samples either dry or coated with varying amounts of oil. **(B)** PFA tube arrangement used to enable bubbling of continuous flow hp^{129}Xe into the liquid oil sample. Gas flow was stopped after approximately 30 s prior to the NMR relaxation measurements.

hp^{129}Xe dissolved phase uptake experiment (Fig. 1A) an inversion recovery protocol was used for 1D-EXSY that was comprised of an initial 180° inversion pulse (Gaussian shape, 230 us duration) applied selectively on the dissolved phase peak(s) followed by a delay time $\boldsymbol{\tau}$ and a 90° non-selective pulse (68 us duration) for read-out, with 4 averaged scans for each increment with TR = 12s. Four repeat experiments across multiple days were averaged together to produce the final uptake curves. The carrier frequency for the foam-oil system was set between the two dissolved phase peaks at 205.1 ppm and both peaks were inverted. For consistency, the same carrier frequency was used for the oil-free foams.

2D-EXSY. The 2D-EXSY sequence applied under continuous flow hp^{129}Xe is represented in Eq. 1. A train of three depolarization pulses, each separated by a $\tau_d = 100\ ms$ delay, was applied before a recycle delay of $\tau_{RD} = 3s$ to establish a steady state situation [51]. This was followed by a 2-dimensional (2D) EXSY sequence [52] (as shown in bold face in Eq.1). For the 2D-EXSY, an initial rf excitation pulse was followed by the incremented evolution time (t1) of the indirect domain, a second rf pulse, the exchange time τ_{ex}, the final rf pulse and the data acquisition AQ in the direct (t2) domain [4,51,53]. For the measurements the exchange times τ_{ex} ranged from 100 ms to 2000 ms. To reduce the experimental time, the phase cycle was limited to 8 steps where the phase θ_1 was altered between 0° and 180° for axial peak suppression. In addition, θ_2 was incremented in four steps by 90°.

$$\{\tau_d - (\pi/2)_0\}_3 - \tau_{RD} - (\boldsymbol{\pi}/2)_{\boldsymbol{\theta}_1} - \boldsymbol{t1} - (\boldsymbol{\pi}/2)_0 - \boldsymbol{\tau_{ex}} - (\boldsymbol{\pi}/2)_{\boldsymbol{\theta}_2} - \boldsymbol{AQ}(\boldsymbol{t2}) \quad (1)$$

However, to obtain a meaningful spectral resolution over the full 230 ppm range, a high number of (small) t1 increments was required that would have resukted in long experimental times under continuous flow conditions and therefore high xenon consumption. Instead, a smaller spectral window of 120.1 ppm x 120.1 ppm was used to intentionally violate the Nyquist condition, thereby causing spectral folding (folding-in) of the gas phase peak to 241.5 ppm. The presented 2D-spectra are the results from 8 averaged scans, centre frequency at 186.1 ppm, with 128 t1 increments (resolution 256 × 128), zero filled to 512 × 256 and cropped to the spectral region of interest. Depending on the selected exchange time, each 2D-EXSY measurement took between 60 and 90 min to complete eight averaged scans. The duration of the rf pulses was 40 μs and hence, sufficiently short to cover the dissolved phase while the gas phase was not experiencing full excitation. Therefore, the relative intensities of the dissolved phase versus gas phase signals do not reflect the true quantitative signal ratios and the purpose of the 2D-EXSY was solely to exhibit the order of exchange between gas and the two dissolved phases qualitatively.

Pure oil phase spectroscopy and T_1 measurements. To measure the behaviour of hp^{129}Xe dissolved in oil, the setup of Fig. 1B was utilized with gas bubbling through the liquid for 30 s to diminish paramagnetic oxygen for the relaxation measurements and to obtain a near steady state dissolved phase hp^{129}Xe signal. After flow interruption, the chemical shift was measured after a single 90° pulse. For the longitudinal (T_1) relaxation measurement, a train of small $\theta = 9°$ flip angle pulses was applied, each separated by a time delay τ [54,55]. The elapsed time t after the nth pulse was $= (n-1)\tau$. The T_1 time was calculated from the decay of the signal intensity as a function of experimental time $S(t)$ using Eq. 2 that takes the depolarization from the rf pulse with flip angel θ into account and where the pulse number is expressed by the total experimental time t divided by the inter-pulse delay τ [55,56]. S_0 is the initial signal intensity for $t = 0$.

$$S(t) = S_0 \cdot \sin(\theta) cos^{(t/\tau)}(\theta) \cdot e^{-t/T_1} \quad (2)$$

Hp^{129}Xe MRI of dissolved phase phantom at 1.5 Tesla. MRI of the phantom were obtained using a clinical 1.5T whole body MRI scanner (GE HDX13) with a transmit/receive vest coil (Clinical MR Solutions, Wisconsin, USA) resonating at 17.66 MHz (Fig.2D). A commercial hyperpolarizer (Polarean 9800 with upgrade module 3777) was used to fill Tedlar® bags with 1 L concentrated hp^{129}Xe (92 % isotopically enriched) with a hyperpolarization of $P = 12 \pm 1$ % as was measured in the Tedlar® bags before delivery to the MRI scanner and inhalation by the patient. This MRI protocol [33] was identical to the one used previously for a multi-site clinical study in post-COVID lung disease [57].

Fig. 2A depicts 25 mm diameter circular foam discs, cut from the 10 mm thick A4 sheets using a circular blade custom-manufactured from a sharpened stainless-steel tube. The discs were placed dry, or with olive oil at various mass percentages, inside two 260 mm (R-tube) and 254 mm (L-tube) long, 24 mm inner diameter (ID) sample container, custom

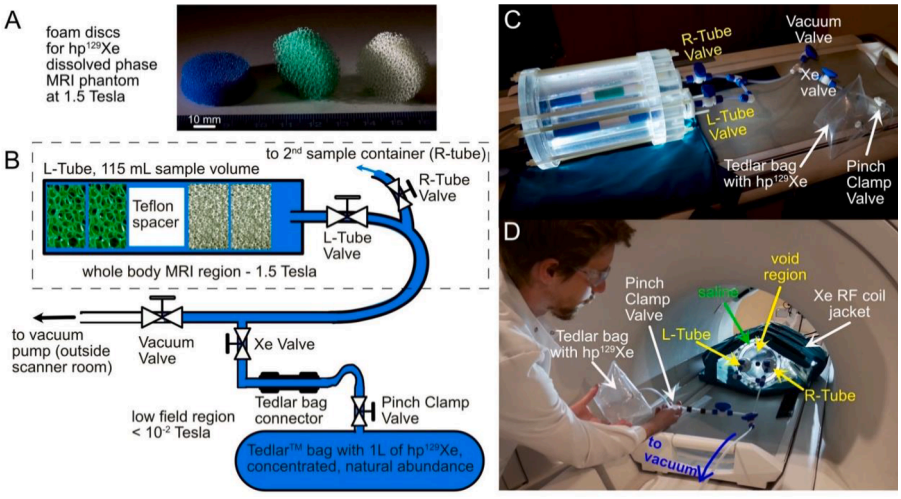

Fig. 2. Setup for the hp^{129}Xe MRI of the dissolved phase phantom in a 1.5 Tesla GE whole body clinical scanner. **(A)** Foam discs with 25 mm diameter and 1 cm thickness were cut from sheets of (from left to right): ZR45H-blue, ZR20H-green, and ZR30H-beige. **(B)** Sketch of one of the 24 mm ID sample containers with various 25 mm diameter foam discs (slightly squeezed to fit), a Teflon spacer with 22 mm diameter to allow free gas passage, and free gas space. The sample container was connected via ¼" PFA tubing to the gas delivery manifold that enabled evacuation of the sample space and delivery lines and hp^{129}Xe delivery from a 1 L Tedlar® bag via pressure equalization to ambient pressure. **(C)** Photograph of the setup featuring two sample containers (L-Tube and R-Tube) with individual shut-off valves (not used in this work) and the gas delivery manifold. The sample containers were placed in parallel with their centre axes 10 cm apart inside a larger, 21 cm OD container with a 1.5 cm wide cylindrical outer region for 1 L of physiological saline solution. **(D)** Photograph of in situ operational conditions during MRI scanning. The phantom was, together with three additional saline bags, placed inside a flexible body coil for excitation and observation of hp^{129}Xe at 17.66 MHz.

made from Perspex™ with an internal volume of approximately 115 mL each. A removable double O-ring sealed Teflon plug with a ¼" tubing outlet connects the container volume to a PFA transfer line via a Swagelok™ link. The sketch in Fig. 1D outlines the protocol for phantom usage. Initially, the sample tubes, placed inside the 1.5 T MRI whole body magnet were evacuated for a few minutes with the Xe Valve closed. A Tedlar® bag (Jensen Inert Products, USA) with ¼ Jaco fittings was filled with 1 L hp^{129}Xe and attached, as shown in Figs. 2B and C, to the manifold made from ¼" diameter PFA tubing and various Swagelok PFA connectors. All valves were PFA plug valves with ¼" Swagelok tube fittings, except for the Pinch Clamp Valve at the Tedlar® bag. The Xe Valve was opened, with the Pinch Clamp Valve closed, to evacuate the connector region for about 1 min via PFA to a standard vacuum pump (RV3 two stage rotary vane vacuum pump by Edwards, Atlas Copco Group, Sweden), located outside the scanner room. The Vacuum Valve was then closed, followed by opening the Pinch Clamp Valve to allow for hp^{129}Xe transfer into the sample region (through pressure equalization) to ambient pressure. This was followed by the MRI acquisition, in complete analogy to the clinical protocol, except that oxygen was largely absent in the phantom resulting in prolonged relaxation times, T_1 gas $>>$ 15s. Furthermore, the total volume of the two sample containers was only about 230 mL, and therefore one Tedlar® bag with 1 L hp^{129}Xe was able to comfortably provide the contrast agent for two further experiments after renewed evacuation and transfer procedure.

Fig. 2D shows photographs of the actual setting with both sample tubes located in a 21 cm outer diameter (OD) container that contained a cylindrical ring chamber with 1 L of physiological saline solution to facilitate ^{1}H localizing scans and to ensure that the LC-circuit of the coil was matched in the absence of a patient. For the same reason, three additional 1 L saline bags were placed inside the coil region.

3. Results and discussion

3.1. Polymer foams with dissolved phase hp ^{129}Xe signal emulating the red blood cell (RBC) signal

Reticulated polyurethane foam, utilized in a separate study investigating flow in porous media [58], was identified as a polymer that dissolves xenon with a chemical shift signature similar to that of RBC. For the current study, eight different polyurethane foams (see experimental section) were tested for its dissolved phase ^{129}Xe chemical shift using the setup described in Fig. 1A. The resulting hp^{129}Xe spectra of three particular polymers (ZR20H-green, ZR30H-beige, ZR45H-blue), shown in Fig. 3, displayed a 215± 0.7 ppm shift (line width of 6.2 ± 0.2 ppm) that is reasonably close to the typical pulmonary RBC chemical shift range of 219–218 ppm and typical RBC linewidths of about 10 ppm [5,14,15]. Only these three foams were further investigated in this work. The other reticulated polyurethane foams were found to have a less favourable chemical shift at 208 ppm.

The observed dissolved phase peak intensity, normalized by the gas phase signal intensity $\boldsymbol{I_{dp}(TR)/I_{gas}}$ was strongly dependent on the time period between scan ($\boldsymbol{TR} = 5\boldsymbol{s}$ in Fig. 3) that allowed for 'fresh' gas phase hp^{129}Xe to replace the dissolved phase xenon in the polymer after depolarization of the dissolved phase by the previous 90° pulse. The gas phase intensity $\boldsymbol{I_{gas}}$ showed little time dependence due to chemical shift selective excitation of the dissolved phase and the continuous flow conditions in the gas phase. Independent of TR, the intensity in a particular polymer is a function of the polymer surface to gas volume ratio (S_P/V_G) but also by the xenon solubility in the material. The strongest relative polymer hp^{129}Xe signal in Fig. 3 was observed with ZR45H-blue.

To study the timescale of the xenon dissolution, a 1D exchange spectroscopy (1D-EXSY) sequence was adapted from the inversion recovery protocol for T_1 relaxation measurements with three distinctions: (1) The 180° pulse was (dissolved phase) chemical shift selective; (2) relaxation could not cause signal recovery of a hyperpolarized system; (3) instead, the signal recovery, shown in Fig. 4 was a function $\boldsymbol{\tau_{ex}}$ and therefore was not a 'relaxation recovery' but an 'exchange recovery' due the replacement of depolarized dissolved phase ^{129}Xe by hp^{129}Xe from the gas phase. This concept is in analogy to previous pulmonary spectroscopic work to study the hp^{129}Xe uptake kinetics in lungs [20], albeit under continuous flow conditions. Similarely, 1D-EXSY hp^{129}Xe experiments using continuous flow that was interrupted briefly through trigger pulses during the NMR scans have also very successfully been applied to explore the exchange kinetics in cryptophane–xenon host–guest systems [59].

The time dependence of the dissolved phase hp^{129}Xe signal was a function of the diffusion driven mean displacement of the xenon atoms into deeper layers of the polymer:

$$\boldsymbol{I_{dp}(\tau_{ex})/I_{gas} = C^{ex}\sqrt{6D_{dp}\tau_{ex}}} \quad (3)$$

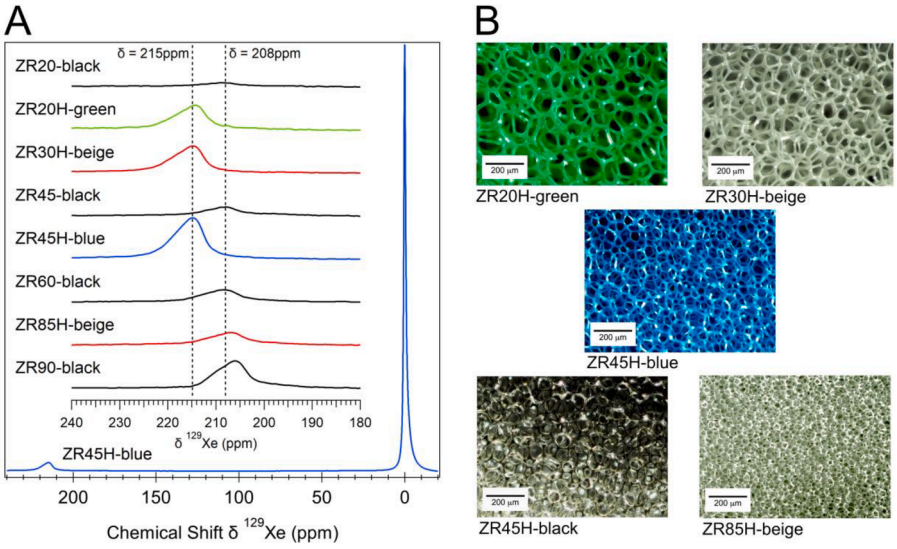

Fig. 3. **(A)** Hp ^{129}Xe NMR spectra showing dissolved phase peaks of various polyurethane foams in the 206 – 215 ppm range. The hp^{129}Xe was allowed to penetrate for 5 s into the materials between depolarizing 90° pulses. The dissolved phase peak intensities were normalized to the respective gas phase signal. The complete spectral range, including the gas phase peak at 0 ppm, is shown at the bottom for ZR45H-blue. **(B)** Micrographs of the various polyurethane foams as indicated in the figure.

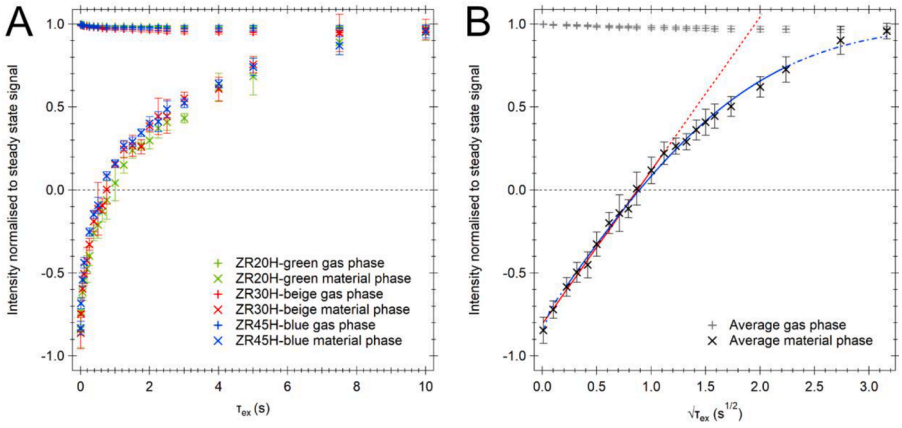

Fig. 4. **(A)** Signal build-up, $I_{dp}(\tau_{ex})/I_{dp}(10s)$, as a function of time ('x' symbols) for various polymer foam samples with dissolved phase resonances between 215 and 214 ppm. Also shown is the gas phase intensity, normalized to the gas phase intensity at $\tau_{ex} = 0s$ ('+' symbols), that displays intensities with little change and close to unity as the continuous flow of hp ^{129}Xe replaced the depolarized gas. **(B)** Signal build up, $I_{dp}(\tau_{ex})/I_{dp}(10s)$, of the averaged data from all foams in (A) as a function of $\sqrt{\tau_{ex}}$. Fitting of the region $0.1s^{1/2} < \tau_{ex}^{1/2} < 1.1s^{1/2}$ to Eq. 3 indicates $\sqrt{\tau_{ex}}$ dependence shown by the solid red straight line (with red dotted line extension showing extrapolation beyond the fitting region). Fitting to Eq. 4., shown as black line (with solid line indicating the fitting region and the dash-dotted line indicating extrapolation), resulted to $T_1 = 4.6 \pm 1.8$ s. All I_{dp}/I_{gas} data was obtained from signal height, but data from integrated signal intensities yielded very similar results. Note that the data was normalized to steady-state signal measurement attained prior to each 1D-EXSY repeat experiment.

where D_{dp} is the diffusion constant of dissolved phase xenon in the polymer, and τ_{ex} is the exchange delay time and the pre-factor C^{ex} is a parameter describing the exchange of the xenon from the gas phase into the material that was dependent on S/V, the xenon partial pressure (or xenon density), and the xenon solubility in the polymer. Like xenon uptake in lungs [20], exchange between gas phase and surface likely occured very rapidly, and the time dependence of C^{ex} can be neglected, leaving diffusion as the remaining factor for the time dependence of the hp^{129}Xe signal growth.

To study the diffusion properties independent of S/V, the signal intensities $I_{dp}(\tau_{ex})$ in Fig. 4 were normalized to the steady state signal after 10 s of uptake. The hp^{129}Xe signal uptake in Fig. 4B is displayed as a function of $\sqrt{\tau_{ex}}$ demonstrating that the (near) linear dependence was only present for $\tau_{ex}^{1/2} \leq 1.1s^{1/2}$. For longer times τ_{ex}, the T_1 relaxation caused deviation from the $\sqrt{\tau_{ex}}$ behaviour due to depolarization of the dissolved hp^{129}Xe until the signal reached maximum intensity at steady state. Taking into account the initial inversion pulse, the time dependence of the dissolve phase signal in Fig. 4 is described by [60]

$$I_{dp}(\tau_{ex})/I_{dp}(10s) = (1+A)B\int_0^{\tau_{ex}} \frac{1}{\sqrt{t}} e^{-\frac{t}{T_1}} dt - A, \quad (4)$$

where A is a fitting parameter with $|A| \leq 1$ that takes incomplete signal inversion into account and the factor $B = \left\{ \int_0^{\infty} \frac{1}{\sqrt{t}} e^{-\frac{t}{T_1}} dt \right\}^{-1}$ serves as normalization. Unfortunately, it is very difficult to determine the T_1 time within the foam independently, however, fitting the average material phase uptake resulted in a $T_1 = 4.6 \pm 1.8$ s. To achieve this, the data presented in Fig. 6.4B, was numerically differentiated using the central difference method (approx. endpoints), before fitting with Eq. 5 that is the time derivative of Eq. 4:

$$\frac{d}{dt} I_{dp}(\tau_{ex})/I_{dp}(10s) = C\frac{1}{\sqrt{\tau_{ex}}} e^{-\frac{\tau_{ex}}{T_1}} \quad (5)$$

where C is a constant. The data endpoints were omitted from this fitting as they were approximated during the numeric differentiation step using a forward difference for the first point and a backward difference for the last point. The best fit was found by removing one further data point from each end. Parameters attained from this fitting procedure were then used to produce a fitting curve of $\frac{d}{dt} I_{dp}(\tau_{ex})/I_{dp}(10s)$, which was then integrated using the trapezoidal rule for numeric integration to produce the fitted curve of Eq. 4.

3.2. *Mimicking the pulmonary dissolved phase hp ^{129}Xe signal, M, through olive oil*

To emulate the 197 ppm of hp ^{129}Xe signal in the pulmonary M phase, olive oil was utilized because it exhibits a reported 198 ppm ^{129}Xe chemical shift at 296.7 K (23.5 °C) with −0.2ppm/K temperature dependence [61]. Fig. 5A shows a spectrum obtained from the bulk liquid phase at 195.7 ppm ± 0.3 ppm, a slightly lower value than expected at the measurement temperature of 293 K (20 °C) and the resulting spectra when using varying mass percentages of olive oil on the foam. The dissolved phase ^{129}Xe NMR frequency (195.7 ± 0.5 ppm) was little affected by the applied amount of oil, however the intensity ratio $I_{dp-oil}(TR = 5s)/I_{gas}$ increased with increasing mass percentage.

Unlike clinical hp^{129}Xe MRI, that uses cryogenic freeze-thaw separation to increase the concentration of xenon, a dilute 5 %:95 % Xe:N_2 gas mixture was used for the NMR spectroscopy in this study. To verify that dilution will not affect the spectral profile, pure (100 %) xenon was extracted after SEOP through cryogenic separation. No significant effect was observed for the dissolved phase chemical shift in Fig. 5A (except for the expected approximate ½ ppm gas phase shift) [10,11]. However, increasing the temperature by 10 K reduced the dissolved phase shifts by about 2.3 ppm in the polymer as expected from previous polymer studies [62,63] and to a shift by about 2.0 ppm in olive oil [61]. Finally, vacuum pump oil was also tested, as it would fulfil condition (F), however at 293 K the 200.8 ppm ± 0.2 ppm dissolved phase ^{129}Xe NMR shift was far off target.

Fig. 5B shows $I_{dp}(\tau_{ex})/I_{dp}(10s)$ obtained from the 1D-EXSY as a function of $\sqrt{\tau_{ex}}$ for the oil treated polyurethane sample ZR45H-blue at 3 different oil mass ratios. The observed uptake of hp^{129}Xe in the 195.7 ppm oil phase is shown by the filled symbols (i.e. top three curves) and the uptake into the polyurethane material at 215 ppm is indicated by open symbols. The initial uptake into the polyurethane shown in Fig. 5C, is proportional to $\sqrt{\tau_{ex}}$ for $\tau_{ex}^{1/2} \leq 1.1s^{1/2}$ and the pre-factor (i.e. slope) is only slightly reduced by an increasing oil weigh ratio, most likely caused by decreasing polymer S/V ratio with increasing oil content that is only partially offset by the normalization with the steady state signal.

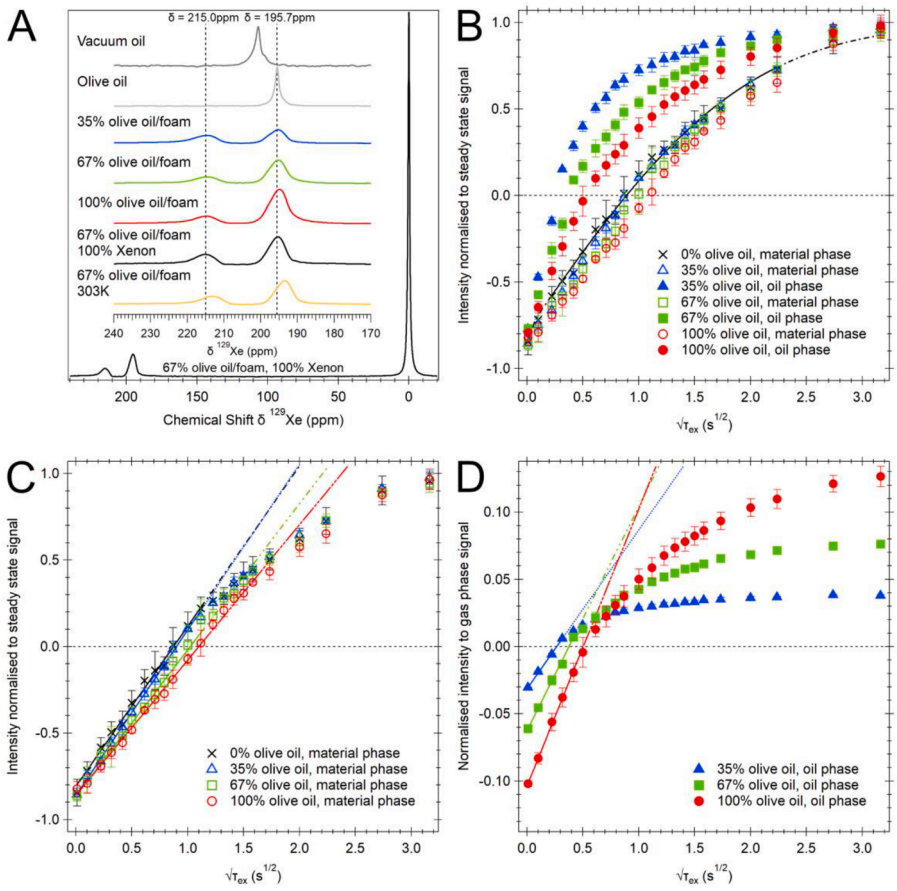

Fig. 5. **(A)** Hp ^{129}Xe NMR spectra of bulk liquid vacuum oil, olive oil, and olive oil on ZR45H-blue foam at various mass percentages (i.e. oil mass divided by the mass of oil free foam) using a 5 % Xe: 95 % N_2 mixture for continuous flow SEOP and detection at 293K. Spectra resulting from pure (100 %) Xe and from 5 % Xe but at 303 K (30 °C) for the 67 % olive oil - foam sample are also shown. Full spectral range from gas phase to dissolved phases for the 67 % olive oil - foam depicted at the bottom. **(B)** Hp^{129}Xe uptake, $\boldsymbol{I_{dp}(\tau_{ex})/I_{dp}(10s)}$, in oil covered foam samples (ZR45H-blue) after selective inversion of the two dissolved phase peaks as a function of $\sqrt{\tau_{ex}}$ for various oil-foam mass percentages. Filled symbols (top three curves) show the uptake into the oil phase and open symbols (3 lowest curves) show the uptake into the polyurethane material. Black "x"s represent the averaged uptake data from the oil free foams from Fig. 4B. **(C)** Fitting of all polymer uptake curves of hp^{129}Xe in the polymer. **(D)** Hp^{129}Xe uptake in oil but normalized to gas phase peak indicating the same initial uptake behaviour. Note that the data was normalized to steady-state signal measurement attained prior to each 1D-EXSY repeat experiment.

The initial hp^{129}Xe uptake in the oil phase was also proportional to $\sqrt{\tau_{ex}}$ but, due to the slow ^{129}Xe relaxation in olive oil ($T_1 = 20.8 \pm 0.9$ s – see methods section, '*Pure oil phase spectroscopy and T_1 measurements.*') the deviation from $\sqrt{\tau_{ex}}$ behaviour at $\boldsymbol{\tau_{ex}^{1/2} \geq 0.4 s^{1/2}}$ was likely caused by saturation of the oil with the dissolved gas, similar to previous observations in lung tissue [20]. In contrast to the uptake in the polymer, the uptake slope in oil in Fig. 5B was strongly dependent on the amount (mass percentage) of oil placed onto the foam. The decreasing slope with increasing oil percentage was a consequence of the normalization to $\boldsymbol{I_{dp}(10s)}$ as samples with low oil contents were closer to the steady state saturation point than those with high oil mass percentage. Low oil content samples had therefore a faster initial fractional increase in hp^{129}Xe. However, when the uptake signal was normalized to the gas phase signal, as displayed in Fig. 5D, the situation reversed with lower oil content samples displaying a slower initial increase, most likely due to lower S/V ratios.

The hp^{129}Xe uptake behaviour in oil was further explored in Fig. 6(B, D, and F) where a sample tube was half filled with bulk liquid olive oil while the container wall of the upper half was coated with a thin film of the oil. Due to the orientation dependence of bulk magnetic susceptibility, hp^{129}Xe entering the surface region of the bulk liquid (surface normal parallel to the magnetic field lines) resonated at 200.2 ± 0.2 ppm in comparison to the 193.3 ± 0.2 ppm of hp^{129}Xe dissolved in the oil coated surface (surface normal perpendicular). This allowed for a straightforward distinction between the two phases, revealing that the normalized surface oil signal (iii) rose faster than the normalized bulk phase signal (ii) due to the faster saturation of the thin layer of wall oil with hp^{129}Xe, thereby confirming the interpretation for Fig. 5.

3.3. *Continuous flow hp^{129}Xe 2D-EXSY NMR spectroscopy of the polymer-oil system*

2D EXSY NMR spectroscopy is shown in Fig. 7 to provide a better understanding of the pathways of the hp^{129}Xe within the foam-oil system. To reduce the experimental time (see experimental section), the Nyquist condition was intentionally violated leading to a folding in of the gas phase peak at 241.5 ppm.

The strongest cross peak in Fig. 7 is between the gas phase at 241.5 ppm and the oil at 195.7 ppm but there is no cross peak indicating transport from the oil phase back into the gas phase. Likewise, the second strongest cross peak describes exchange from the gas phase to the polymer dissolved phase at 215.0 ppm, but not the return into the gas phase. This asymmetry in the 2D-EXSY spectra in Fig. 7, usually not observed in 2D-EXSY spectra of thermally polarized spin systems, was a consequence of hyperpolarization and the continuous flow conditions that lead to a net transport of hp^{129}Xe from the gas phase into the material [51,53]. In Fig. 7 it may also have been partially caused by the spectral folding. Symmetric cross peaks exist between the two dissolved

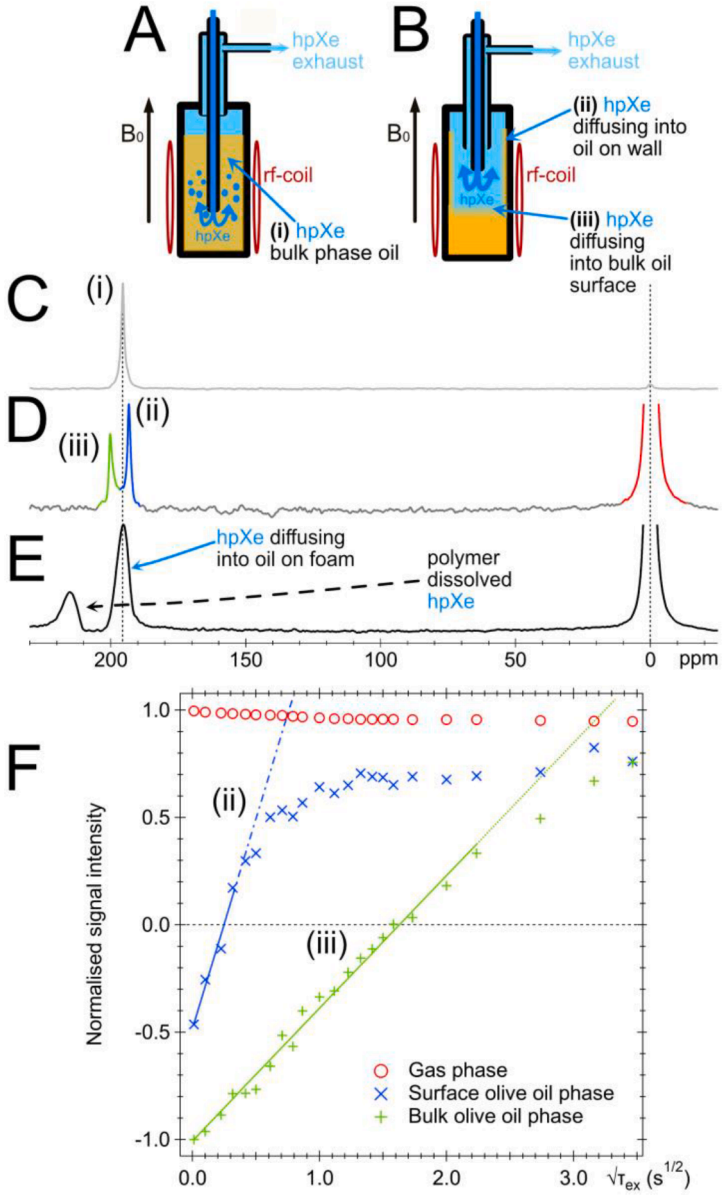

Fig. 6. $Hp^{129}Xe$ NMR of pure olive oil. **(A)** Sketch of sample container for $hp^{129}Xe$ dissolved in oil bulk phase with **(C)** resulting spectral line (i) at 195.7 ppm, recorded after flow interruption. **(B)** Container partially filled with bulk olive oil and a thin layer of oil on the container wall at the top region. Unlike (A & C), the gas was not directed through the oil but was continuously flowing above the liquid and resulted in **(D)** two dissolved phase peaks due to magnetic susceptibility differences of $hp^{129}Xe$ environment. When dissolved within the oil on the container wall (ii) $hp^{129}Xe$ resonated at 193.3 ppm while within the surface region of the bulk oil (iii) it resonated at 200.2 ppm. **(E)** $Hp^{129}Xe$ NMR spectrum of foam-oil system (ZR45H-blue with 67 % oil/foam ratio). **(F)** $Hp^{129}Xe$ uptake, $\boldsymbol{I_{dp}(\tau_{ex})\ /I_{dp}(10s)}$ as a function of $\sqrt{\tau_{ex}}$, obtained using the setting of (B). The bulk oil phase (iii) followed Eq. 3 uptake behaviour for $\tau_{ex}^{1/2} \leq 2.2s^{1/2}$, while the uptake in oil located on the wall (ii) displayed gas saturation effects at short $\sqrt{\tau_{ex}}$ values (Eq. 3 fitted region: $\tau_{ex}^{1/2} \leq 0.3s^{1/2}$**)**. Note that the data was normalized to steady-state signal measurement attained prior to each 1D-EXSY repeat experiment.

phases but with an intensity that is substantially less than of the cross peaks with the gas phase. This indicates that the major mode of gas exchange was from the gas phase directly into oil and polymer materials. This finding is corroborated by the micrograph in Fig. 8 which shows that the oil (dyed red) accumulated as droplets in crossing points of the foam structure leaving other parts of the structure with an accessible polyurethane surface that was directly exposed to the gas phase. Unlike pulmonary gas exchange through the parenchyma into RBC, exchange from the oil into the polymer in this particular phantom material had little effect on the net build-up of the 215.0 ppm peak.

$Hp^{129}Xe$ dissolved phase MRI of the foam-oil phantom with clinical 1.5T whole body scanner. Following the spectroscopic characterization of $hp^{129}Xe$ in the foam-oil system, the phantom material was tested with a dissolved phase $hp^{129}Xe$ MRI protocol from a previous clinical long-COVID study [57]. Fig. 9A details the loading of the sample. The R-tube was filled with discs of the three foams having a $hp^{129}Xe$ dissolved phase chemical shift between 214 and 215 ppm, separated by Teflon spacers from each other. The L-Tube was filled with ZR45H-blue foam only; however, with two different oil mass percentages that were separated by a Teflon spacer. A void space at one end provided a region with bulk gas phase only. Fig. 9B shows the resulting chemical shift selective MRI of the gas phase, M phase (i.e. $hp^{129}Xe$ in oil), and RBC phase (i.e. $hp^{129}Xe$ in the polyurethane).

A first visual inspection of the X,Y slices of the 3D MRI reveals a clear separation between the three phases with the gas phase extending into the void space of the L-tube. The M phase is clearly visible for the L-tube

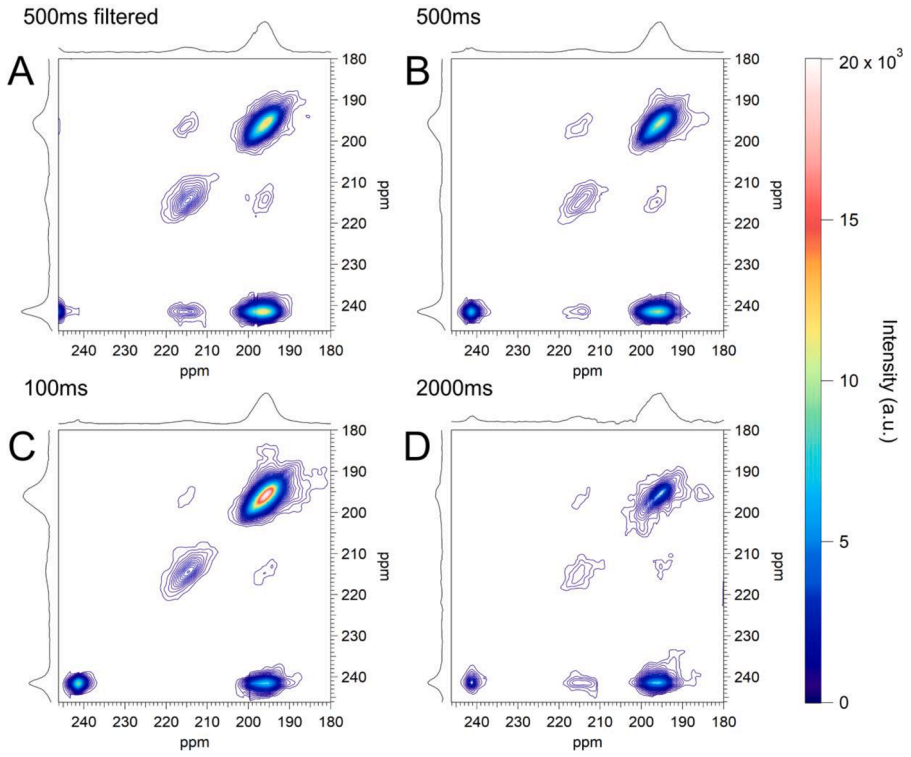

Fig. 7. $Hp^{129}Xe$ 2D-EXSY NMR spectra of the foam/oil system using **ZR45H-blue** with 100 % oil/foam mass ratio. The spectra were cropped from recorded spectra with a range from 180.0 ppm to 246.2 ppm that violate the Nyquist condition, causing a folded-in gas phase peak at 241.5 ppm. **(A)** $Hp^{129}Xe$ 2D-EXSY NMR with an exchange time of $\tau_{ex} = 500$ ***ms*** using a standard digital filter ('sharp') in the frequency domain that removed the folded-in diagonal gas phase peak but cross peaks are visible that indicate exchange from the gas phase to the dissolved phases. Some intensity appears at the spectral edges (i.e. here at 246 ppm and, outside the cropped region at 126 ppm). **(B)** Same as (A) but with the digital filter switched off. The folded-in 240 ppm gas phase peak becomes visible. **(C)** Same protocol as in (B), but with $\tau_{ex} = 100$ ***ms*** and **(D)** with $\tau_{ex} = 2000$ ***ms***.

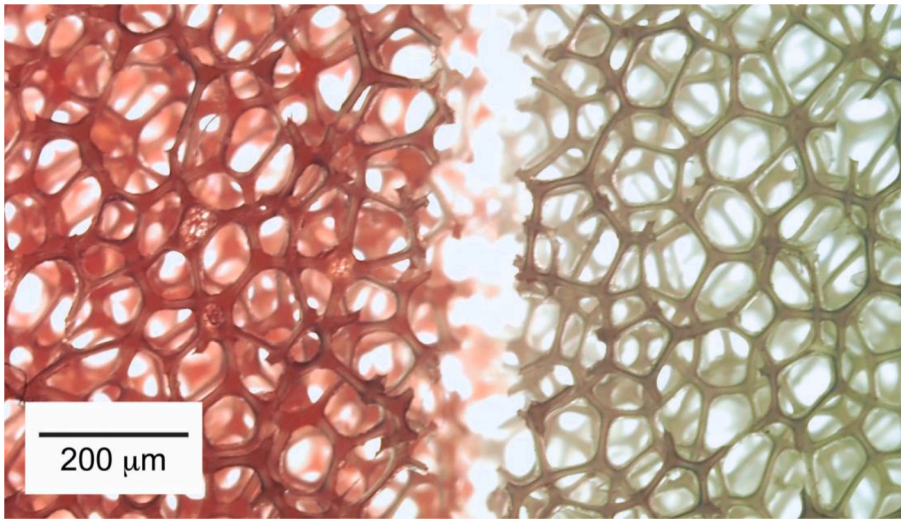

Fig. 8. Micrograph of ZR30H-beige foam, oil free (right) and loaded with 100 % (mass percentage) of olive oil containing a red dye (left). Note that the majority of the oil appears to have accumulated largely in droplets located at the intersection of the polymer strands. This left much of the polymer either coated with only a very thin oil layer or completely exposed to the gas phase.

that contains the oil covered foam, while no signal was detected in the R-tube with the oil-free foams. The M signal from the 100 % oil-foam region appeared stronger than that from the 36 % oil-foam region (L-tube). The RBC phase in the oil-free foams (R-tube) was visibly strongest in ZR45H-blue, while the intensity from the other two foams was not distinguishable by visual inspection.

Ratio maps produced using the gas, M and RBC phase images from slice 16 in Fig. 9B, and the resulting boxplots are presented in Fig. 10. Comparing the RBC/gas ratios in Fig. 10(A&D), the difference between the various oil-free foams (R-tube) was much more pronounced than between the oil and oil-free ZR45-blue foams. The highest RBC/gas ratio was measured for the ZR45H-blue foam and the lowest for ZR20H-green as expected from the polymer surface-to-gas volume ratio (S_P/V_G) and the $hp^{129}Xe$ NMR spectroscopic data. The ZR45H-blue foam with 36 %

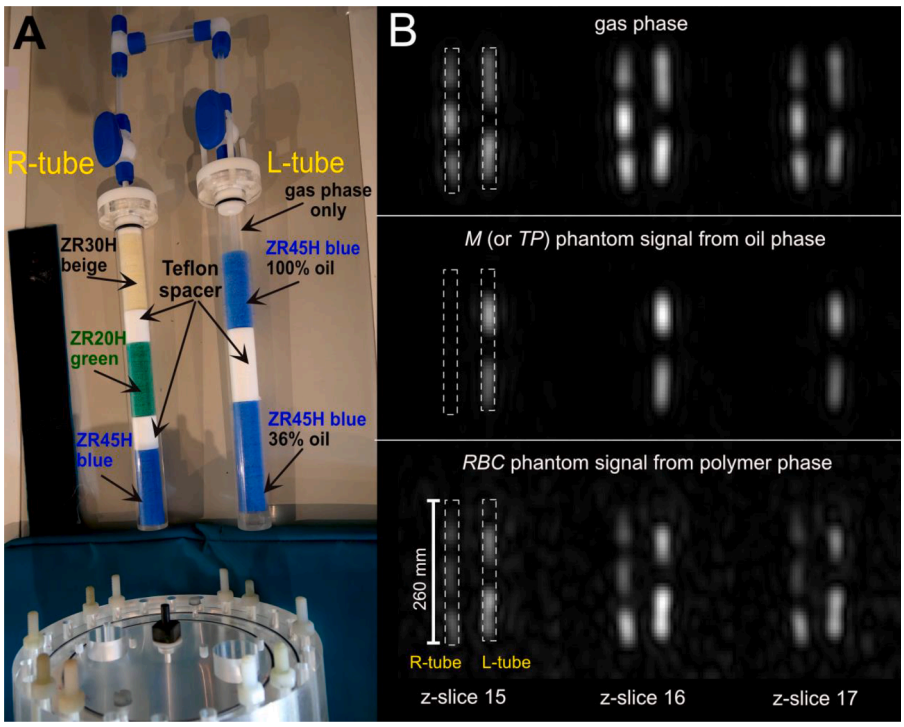

Fig. 9. (A) Photograph of the dissolved phase phantom. R-Tube (260 mm internal length, 24 mm inner diameter) loaded with 7 discs of ZR45H-blue, a 25 mm Teflon spacer, 7 discs of ZR20H-green, followed by another 25 mm Teflon spacer, and by 7 discs of ZR30H-beige. L-Tube (254 mm x 24 mm) loaded with 10 discs of ZR45H-blue containing 36 % (mass percentage olive oil), followed by a 30 mm Teflon spacer, followed by 7 discs of ZR45H-blue containing 100 % (mass percentage) olive oil, and a final free gas space of 4 cm. **(B)** 1.5 T MR images of the gas phase, the olive oil phase signal representing the M (or TP) phase caused by tissue dissolved $hp^{129}Xe$ in lungs, and $hp^{129}Xe$ dissolved in polyurethane representing the RBC phase. The three centre slices (15–17 from 32 total) that fell into the region of the small phantom are shown. The sample container dimensions are indicated for slice 15 (white dashed line). Xenon gas was delivered via the attached gas manifold from a Tedlar® bag that was filled with 1 L of concentrated, 92 % isotopically enriched $hp^{129}Xe$ with $P = 12$ %. Approximately 250 ml of this gas was used to fill the two phantom containers and the connecting tubing to ambient pressure for the MRI scans.

oil contents had a slightly stronger RBC/gas ratio than the ZR45H-blue sample without oil, perhaps this was because of a bit stronger compression due to the presence of oil compared to the dry foam, thus leading to a slightly higher S_P/V_G. However, the 100 % oil coated ZR45H-blue foam exhibited a slightly reduced RBC/gas ratio compared to the oil-free ZR45H-blue foam. This reduction was probably due to the larger quantity of oil that covered a larger proportion of the polymer surface, leading to a reduced exchange between gas and polymer. This reduction is qualitatively in line with the different build-up behaviour in Fig. 5B where the presence of oil reduced the material peak uptake rate. Most significantly, the RBC/gas ratios around 0.002 found with ZR45H-blue were close to the 0.003 – 0.004 range observed in healthy volunteers [43].

As expected, the M/Gas ratios in Fig. 10(B&E) were strongly dependent on the quantity oil that directly related to the signal intensity of the M phase while the gas phase signal remained constant. M/Gas ratio of the 36 % oil sample was remarkably similar to the M/Gas ratio range found in healthy volunteers that approximately falls between 0.006 and 0.01 [43].

Lastly, the M/RBC ratio of about 0.4 observed with ZR45H-blue foam containing 36 % oil in Fig. 10(C&F) was again very similar to that of human volunteers (also around 0.4) [43]. The 100 % oil sample reflected qualitatively a M/RBC ratio reduction that would be expected in severe fibrotic conditions. [33,38,39]

4. Conclusions

With specific consideration to the *conditions A – G* laid out in the introduction, this work reports a phantom and standard concept for $hp^{129}Xe$ dissolved phase pulmonary MRI. A first-generation dissolved phase MRI lung phantom was manufactured from benign materials that pose no health risks and that can readily be utilized in a clinical environment (*condition F)*. The manifold described in this work enabled $hp^{129}Xe$ gas handling protocols that was very similar to those with patients or healthy volunteers but without regulatory (clinical governance approval process) limitations (*condition E*).

The investigated polyurethane-oil system exhibited a ^{129}Xe chemical shift similar to that of the M and RBC phases in the human lung (*condition A*). Furthermore, an $hp^{129}Xe$ dissolved phase protocol for pulmonary MRI at 1.5T previously used in a clinical trial, produced M/Gas, RBC/Gas and RBC/M ratios in the phantom that were similar to those in humans found during the clinical trial in healthy volunteers (*condition B*) and long-COVID patients (i.e. falling into the remit of condition D). Alterations in the material S/V ratio will allow for future adjustments of the intensity ratios.

Once dissolved in the polymer, the short term $hp^{129}Xe$ uptake (within about 1 s) was governed by diffusion and followed a $\sqrt{t}$ dependence. At longer exchange times, relaxation increasingly limited the further growth of the signal until a steady state signal was reached. The ratio of the oil-gas signals (M/gas), and by extension the ratio of the polymer-oil signals (RBC/M), could be adjusted by the amount of oil added to the polymer. For short time intervals, diffusion was the rate limiting factor for the signal uptake in oil, but for longer times saturation effects were dominating. Relaxation played a lesser role in thin oil layers due to the relatively long $T_1 = 20.9 \pm 0.6$ s and the fast ^{129}Xe uptake in olive oil that caused saturation to be the limiting factor. Generally, both relaxation and saturation may affect the intensity ratios in clinical dissolved phase $hp^{129}Xe$ MRI protocols that utilize small flip angle pulses with short repetition times.

Although the chemical shift in both dissolved phases is only

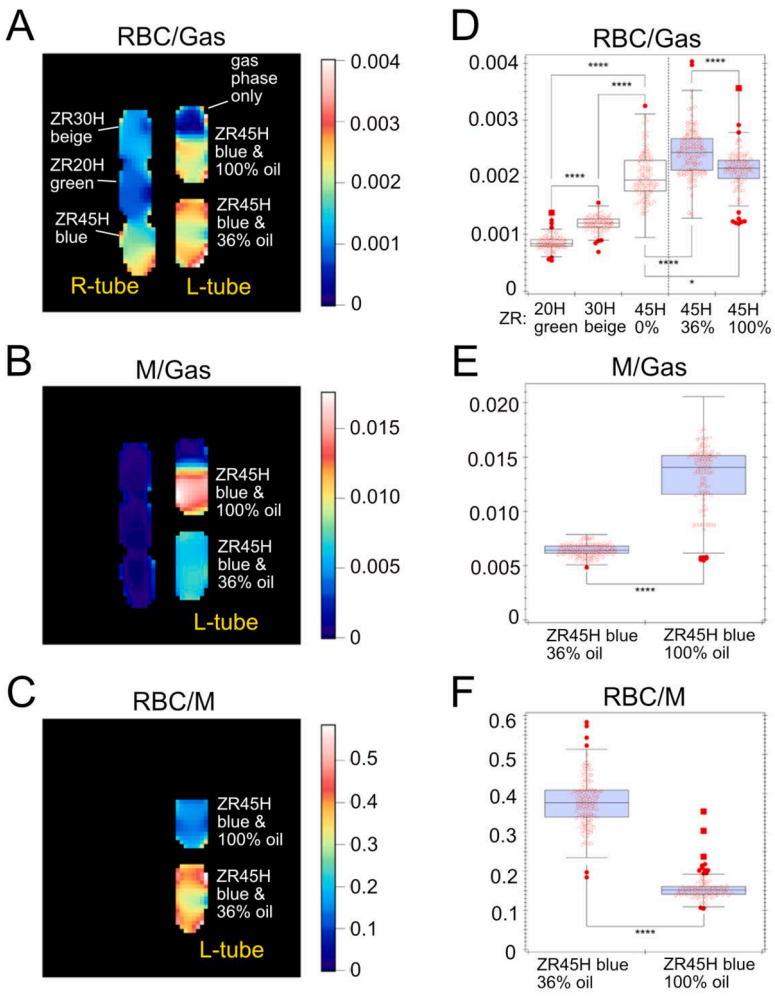

Fig. 10. Ratio maps (A)-(C) and extracted boxplots (D)-(F) obtained from slice 16 of the 3D-MRI data shown in Fig. 9B. All Ratio maps have been masked using a combination of edge detection and image thresholding. Maps (A) and (B) were masked using the gas phase image while map (C) was masked using both the M and RBC phase images. Masks of each ROI (labelled) were then applied to maps (A)-(C) to extract the data for box plots (D)-(F) respectively. Whiskers and outliers were both determined by the Turkey method. Red markers have been added to show all data points used to create each box plot where the open red dots represent data points inside the inner fence, solid red dots represent outliers and solid red squares represent far outliers. Results of the Wilcoxon-Mann-Whitney two-sample rank test are displayed on the boxplots as follows: $p < 0.05$ $(*)$, $p < 0.01$ $(**)$, $p < 0.001$ $(***)$, and $p < 0.0001$ $(****)$, where p in this model represents $p(\textit{two tails})$.

moderately dependent on the small temperature changes expected in a clinical environment, the reproducibility of a future dissolved phase standard may benefit from some temperature control, or for the very least should be outfitted with a low-cost liquid crystal temperature indicator.

Condition (G), requiring long shelf lifetimes, is not yet fulfilled as gravity caused the oil to slowly migrate through the sample, thereby affecting the hp^{129}Xe uptake. This was further exacerbated by slow oil diffusion into the polymer which lead to a small shift in the polymer peak of ^{129}Xe. These effects became apparent after 2–3 weeks but were not further explored. However, if used only for the purpose of cost-efficient training, basic testing of new MRI protocols and the assessment of new hyperpolarizer instrumentation [64,65] prior to their ethical approval, the introduced foam-oil system was found to be sufficiently stable to serve as a qualitative phantom for several months.

As depicted by the slopes in Fig. 5B, the time dependence of the uptake between polymer and oil was different and therefore the observed ratios would be dependent on the pulse timing and flip angles, for example. An understanding of the hp^{129}Xe uptake ratios, as explored extensively in this work, is important to fulfil conditions C & D as changes in the observed signal ratios due to different MRI protocols should follow the same trend in the phantom standard compared to that observed in human lungs. The concepts laid out in this work can be utilized towards the development of a universal standard, for example through additive manufacturing that will allow for phantoms with a longer shelf lifetime but may also include microstructures that mimics the gas transport to - and the exchange kinetics with the pulmonary parenchyma in health and disease.

Declaration of competing interest

The authors declare that they have no known competing financial interests or personal relationships that could have appeared to influence the work reported in this paper.

Acknowledgements

This work was supported by the Medical Research Council (MRC) through [MRC - MR/M008894/1], the MRC Impact Accelerator Award [MRC - MR/X502741/1], and by the Engineering and Physical Sciences Research Council (EPSRC) Impact Accelerator Award [EP/X525765/1]. MF was supported by an EPSRC iCASE PhD studentship [EP/R513283/1], and AH thanks the University of Nottingham for support through the Imaging Beacon of Excellence.

References

[1] Z.Y. Liu, T. Araki, Y. Okajima, M. Albert, H. Hatabu, Pulmonary hyperpolarized noble gas MRI: recent advances and perspectives in clinical application, Eur. J. Radiol. 83 (2014) 1282–1291.

[2] L.L. Walkup, J.C. Woods, Translational applications of hyperpolarized He-3 and Xe-129, NMR Biomed. 27 (2014) 1429–1438.

[3] K. Ruppert, Biomedical imaging with hyperpolarized noble gases, Rep. Prog. Phys. 77 (2014) 116701.

[4] T. Meersmann, E. Brunner, Hyperpolarized xenon-129 magnetic resonance, in: W. Price (Ed.), Developments in NMR, Royal Society of Chemistry, 2015.

[5] H. Marshall, N.J. Stewart, H.F. Chan, M.D. Rao, G. Norquay, J.M. Wild, In vivo methods and applications of xenon-129 magnetic resonance, Prog. Nucl. Mag. Res. Sp. 122 (2021) 42–62.

[6] E.B. Adamson, K.D. Ludwig, D.G. Mummy, S.B. Fain, Magnetic resonance imaging with hyperpolarized agents: methods and applications, Phys. Med. Biol. 62 (2017) R81–R123.

[7] Y.C.T. Huang, M. Wencker, B. Driehuys, Imaging in alpha-1 antitrypsin deficiency: a window into the disease, Ther. Adv. Chronic. Dis. 12 (2021) 20406223211024523.

[8] J.P. Mugler, T.A. Altes, Hyperpolarized 129Xe MRI of the human lung, J. Magn. Reson. Imaging 37 (2013) 313–331.

[9] M. Sharma, P.V. Wyszkiewicz, V. Desaigoudar, F.M. Guo, D.P.I. Capaldi, G. Parraga, Quantification of pulmonary functional MRI: state-of-the-art and emerging image processing methods and measurements, Phys. Med. Biol. (2022) 67, https://doi.org/10.1088/1361-6560/ac9510.22TR01.

[10] D. Brinkmann, E. Brun, H.H. Staub, Kernresonanz Im Gasformigen xenon, Helvetica Physica Acta 35 (1962) 431–436.

[11] A.K. Jameson, C.J. Jameson, H.S. Gutowsky, Density dependence of Xe-129 chemical shifts in mixtures of xenon and other gases, J. Chem. Phys. 53 (1970) 2310, https://doi.org/10.1063/1.1674328. &.

[12] R.S. Virgincar, S.H. Robertson, J. Nouls, S. Degan, G.M. Schrank, M. He, B. Driehuys, Establishing an accurate gas phase reference frequency to quantify ¹²⁹Xe chemical shifts in vivo, Magn. Reson. Med. 77 (2017) 1438–1445, https://doi.org/10.1002/mrm.26229.

[13] J. Wolber, A. Cherubini, A.S.K. Dzik-Jurasz, M.O. Leach, A. Bifone, Spin-lattice relaxation of laser-polarized xenon in human blood, P. Natl. Acad. Sci. U.S.A. 96 (1999) 3664–3669, https://doi.org/10.1073/pnas.96.7.3664.

[14] G. Norquay, G. Leung, N.J. Stewart, J. Wolber, J.M. Wild, Xe chemical shift in human blood and pulmonary blood oxygenation measurement in humans using hyperpolarized Xe NMR, Magn. Reson. Med. 77 (2017) 1399–1408, https://doi.org/10.1002/mrm.26225.

[15] M.S. Albert, V.D. Schepkin, T.F. Budinger, Measurement of Xe-129 T1 in blood to explore the feasibility of hyperpolarized Xe-129 Mri, J. Comput. Assist. Tomo. 19 (1995) 975–978.

[16] Y. Friedlander, B. Zanette, A. Lindenmaier, S. Sadanand, D. Li, E. Stirrat, M. Couch, A. Kassner, R.P. Jankov, G. Santyr, Chemical shift of ¹²⁹Xe dissolved in red blood cells: application to a rat model of bronchopulmonary dysplasia, Magn. Reson. Med. 84 (2020) 52–60, https://doi.org/10.1002/mrm.28121.

[17] K. Ruppert, J.R. Brookeman, K.D. Hagspiel, J.P. Mugler, Probing lung physiology with xenon polarization transfer contrast (XTC), Magn. Reson. Med. 44 (2000) 349–357.

[18] K. Ruppert, J.F. Mata, J.R. Brookeman, K.D. Hagspiel, J.P. Mugler, Exploring lung function with hyperpolarized Xe-129 nuclear magnetic resonance, Magn. Reson. Med. 51 (2004) 676–687, https://doi.org/10.1002/mrm.10736.

[19] H. Imai, A. Kimura, S. Iguchi, Y. Hori, S. Masuda, H. Fujiwara, Noninvasive detection of pulmonary tissue destruction in a mouse model of emphysema using hyperpolarized Xe MRS under spontaneous respiration, Magn. Reson. Med. 64 (2010) 929–938, https://doi.org/10.1002/mrm.22437.

[20] S. Patz, I. Muradyan, M.I. Hrovat, M. Dabaghyan, G.R. Washko, H. Hatabu, J. P. Butler, Diffusion of hyperpolarized (129)Xe in the lung: a simplified model of (129)Xe septal uptake and experimental results, New. J. Phys. 13 (2011) 015009, https://doi.org/10.1088/1367-2630/13/1/015009.

[21] J.D. Fliss, B. Zanette, Y. Friedlander, S. Sadanand, A.A. Lindenmaier, E. Stirrat, D. Li, M. Post, R.P. Jankov, G. Santyr, Hyperpolarized ¹²⁹Xe magnetic resonance spectroscopy in a rat model of bronchopulmonary dysplasia, Am. J. Physiol.-Lung C 321 (2021) L507–L517, https://doi.org/10.1152/ajplung.00612.2020.

[22] J.S. Xie, H.D. Li, H.T. Zhang, X.C. Zhao, L. Shi, M. Zhang, S. Xiao, H. Deng, K. Wang, H. Yang, et al., Single breath-hold measurement of pulmonary gas exchange and diffusion in humans with hyperpolarized ¹²⁹Xe MR, NMR Biomed. 32 (2019) 11, https://doi.org/10.1002/nbm.4068.

[23] H.D. Li, X.C. Zhao, Y.J. Wang, X. Lou, S.Z. Chen, H. Deng, L. Shi, J.S. Xie, D. Z. Tang, J.P. Zhao, et al., Damaged lung gas exchange function of discharged COVID-19 patients detected by hyperpolarized ¹²⁹Xe MRI, Sci. Adv. 7 (2021) 9, https://doi.org/10.1126/sciadv.abc8180.

[24] M. Zhang, H.D. Li, H.C. Li, X.C. Zhao, X.L. Liu, Y.Q. Han, X.P. Sun, C.H. Ye, X. Zhou, Dynamic evaluation of acute lung injury using hyperpolarized ¹²⁹Xe magnetic resonance, NMR Biomed. 37 (2024) 11, https://doi.org/10.1002/nbm.5078.

[25] B. Driehuys, G.P. Cofer, J. Pollaro, J.B. Mackel, L.W. Hedlund, G.A. Johnson, Imaging alveolar-capillary gas transfer using hyperpolarized Xe-129 MRI, P. Natl. Acad. Sci. U.S.A. 103 (2006) 18278–18283.

[26] Z.I. Cleveland, G.P. Cofer, G. Metz, D. Beaver, J. Nouls, S.S. Kaushik, M. Kraft, J. Wolber, K.T. Kelly, H.P. McAdams, et al., Hyperpolarized Xe-129 MR imaging of alveolar gas uptake in humans, PLoS One 5 (2010) e12192.

[27] J.P. Mugler, T.A. Altes, I.C. Ruset, I.M. Dregely, J.F. Mata, G.W. Miller, S. Ketel, J. Ketel, F.W. Hersman, K. Ruppert, Simultaneous magnetic resonance imaging of ventilation distribution and gas uptake in the human lung using hyperpolarized xenon-129, P. Natl. Acad. Sci. U.S.A 107 (2010) 21707–21712, https://doi.org/10.1073/pnas.1011912107.

[28] S.S. Kaushik, M.S. Freeman, S.W. Yoon, M.G. Liljeroth, J.V. Stiles, J.E. Roos, W. M. Foster, C.R. Rackley, H.P. McAdams, B. Driehuys, Measuring diffusion limitation with a perfusion-limited gas-hyperpolarized Xe gas-transfer spectroscopy in patients with idiopathic pulmonary fibrosis, J. Appl. Physiol. 117 (2014) 577–585, https://doi.org/10.1152/japplphysiol.00326.2014.

[29] N.J. Stewart, G. Leung, G. Norquay, H. Marshall, J. Parra-Robles, P.S. Murphy, R. F. Schulte, C. Elliot, R. Condliffe, P.D. Griffiths, et al., Experimental validation of the hyperpolarized Xe-129 chemical shift saturation recovery technique in healthy volunteers and subjects with interstitial lung disease, Magn. Reson. Med. 74 (2015) 196–207.

[30] N.D. Weatherley, N.J. Stewart, H.F. Chan, M. Austin, L.J. Smith, G. Collier, M. Rao, H. Marshall, G. Norquay, S.A. Renshaw, et al., Hyperpolarised xenon magnetic resonance spectroscopy for the longitudinal assessment of changes in gas diffusion in IPF, Thorax 74 (2019) 500–502, https://doi.org/10.1136/thoraxjnl-2018-211851.

[31] J.M. Wang, S.H. Robertson, M. He, R.S. Virgincar, G.M. Schrank, R. Smigla, T. O'Riordan, J. Sundy, L. Ebner, C.R. Rackley, et al., Using hyperpolarized 129xe imaging to quantify apical vs. basal and central vs. peripheral gas exchange impairment in idiopathic pulmonary fibrosis, Am. J. Resp. Crit. Care 193 (2016).

[32] Z.Y. Wang, S.H. Robertson, J. Wang, M. He, R.S. Virgincar, G.M. Schrank, E.A. Bier, S. Rajagopal, Y.C. Huang, T.G. O'Riordan, et al., Quantitative analysis of hyperpolarized Xe gas transfer MRI, Med. Phys. 44 (2017) 2415–2428, https://doi.org/10.1002/mp.12264.

[33] G.J. Collier, J.A. Eaden, P.J.C. Hughes, S.M. Bianchi, N.J. Stewart, N. D. Weatherley, G. Norquay, R.F. Schulte, J.M. Wild, Dissolved ¹²⁹Xe lung MRI with four-echo 3D radial spectroscopic imaging: quantification of regional gas transfer in idiopathic pulmonary fibrosis, Magn. Reson. Med. 85 (2021) 2622–2633, https://doi.org/10.1002/mrm.28609.

[34] J.M. Wang, S.H. Robertson, Z.Y. Wang, M. He, R.S. Virgincar, G.M. Schrank, R. M. Smigla, T.G. O'Riordan, J. Sundy, L. Ebner, et al., Using hyperpolarized Xe MRI to quantify regional gas transfer in idiopathic pulmonary fibrosis, Thorax 73 (2018) 21–28, https://doi.org/10.1136/thoraxjnl-2017-210070.

[35] L.J. Rankine, Z.Y. Wang, J.M. Wang, M. He, H.P. McAdams, J. Mammarappallil, C. R. Rackley, B. Driehuys, R.M. Tighe, ¹²⁹xenon gas exchange magnetic resonance imaging as a potential prognostic marker for progression of idiopathic pulmonary fibrosis, Ann. Am. Thorac. Soc. 17 (2020) 121–125, https://doi.org/10.1513/AnnalsATS.201905-413RL.

[36] Z.Y. Wang, E.A. Bier, A. Swaminathan, K. Parikh, J. Nouls, M. He, J. G. Mammarappallil, S. Luo, B. Driehuys, S. Rajagopal, Diverse cardiopulmonary diseases are associated with distinct xenon magnetic resonance imaging signatures, Eur. Respir. J. 54 (2019), https://doi.org/10.1183/13993003.00831-2019.1900831.

[37] L.C. Saunders, G.J. Collier, H.F. Chan, P.J.C. Hughes, L.J. Smith, J.G.R. Watson, J. E. Meiring, Z. Gabriel, T. Newman, M. Plowright, et al., Longitudinal lung function assessment of patients hospitalized with COVID-19 using 1H and 129Xe lung MRI, Chest 164 (2023) 700–716, https://doi.org/10.1016/j.chest.2023.03.024.

[38] L. Saunders, G. Collier, L. Smith, P. Hughes, H. Marshall, H. Chan, A. Biancardi, J. Grist, S. Strickland, L. Gustafsson, et al., S19Gas exchange imaging using dissolved-phase 129Xe MRI in post COVID cohorts, Thorax 78 (2023) A18–A19, https://doi.org/10.1136/thorax-2023-BTSabstracts.25.

[39] L. Saunders, G. Collier, H.-F. Chan, P. Hughes, L. Smith, H. Marshall, M. Brook, A. Biancardi, M. Rao, G. Norquay, et al., Impaired xenon gas transfer observed two years after COVID-19 hospitalisation in patients with signs of interstitial lung disease, Eur. Respir. J. 62 (2023) OA4857, https://doi.org/10.1183/13993003.congress-2023.OA4857.

[40] K. Ruppert, F. Amzajerdian, H. Hamedani, Y. Xin, L. Loza, T. Achekzai, I.F. Duncan, H. Profka, S. Siddiqui, M. Pourfathi, et al., Assessment of flip angle-TR equivalence for standardized dissolved-phase imaging of the lung with hyperpolarized 129Xe MRI, Magn. Reson. Med. 81 (2019) 1784–1794, https://doi.org/10.1002/mrm.27538.

[41] P.J. Niedbalski, C.S. Hall, M. Castro, R.L. Eddy, J.H. Rayment, S. Svenningsen, G. Parraga, B. Zanette, G.E. Santyr, R.P. Thomen, et al., Protocols for multi-site trials using hyperpolarized ¹²⁹Xe MRI for imaging of ventilation, alveolar-airspace size, and gas exchange: a position paper from the ¹²⁹Xe MRI clinical trials consortium, Magn. Reson. Med. 86 (2021) 2966–2986, https://doi.org/10.1002/mrm.28985.

[42] J.W. Plummer, M.M. Willmering, Z.I. Cleveland, C. Towe, J.C. Woods, L.L. Walkup, Childhood to adulthood: accounting for age dependence in healthy-reference distributions in ¹²⁹Xe gas-exchange MRI, Magn. Reson. Med. 89 (2023) 1117–1133, https://doi.org/10.1002/mrm.29501.

[43] G.J. Collier, L.J. Smith, L.C. Saunders, A.J. Swift, H. Marshall, N.J. Stewart, G. Norquay, P.J.C. Hughes, A.A.R. Thomspson, J.M. Wild, Age, sex, and lung volume dependence of dissolved xenon-129 MRI gas exchange metrics, Magn. Reson. Med. (2024) 13, https://doi.org/10.1002/mrm.30133.

[44] T. Ito, J. Fraissard, Xe-129 NMR-study of xenon adsorbed on Y zeolites, J. Chem. Phys. 76 (1982) 5225–5229.

[45] E.A. Bier, J.C. Nouls, Z.Y. Wang, M. He, G. Schrank, N. Morales-Medina, R. Hashoian, H. Svetlik, J.P. Mugler, B. Driehuys, A thermally polarized Xe

phantom for quality assurance in multi-center hyperpolarized gas MRI studies, Magn. Reson. Med. 82 (2019) 1961–1968, https://doi.org/10.1002/mrm.27836.
[46] Y. Shepelytskyi, V. Grynko, M.R. Rao, T. Li, M. Agostino, J.M. Wild, M.S. Albert, Hyperpolarized ¹²⁹Xe imaging of the brain: achievements and future challenges, Magn. Reson. Med. 88 (2022) 83–105, https://doi.org/10.1002/mrm.29200.
[47] Z.I. Cleveland, R.S. Virgincar, Y. Qi, S.H. Robertson, S. Degan, B. Driehuys, 3D MRI of impaired hyperpolarized Xe-129 uptake in a rat model of pulmonary fibrosis, NMR Biomed. 27 (2014) 1502–1514.
[48] J.S. Six, T. Hughes-Riley, K.F. Stupic, G.E. Pavlovskaya, T. Meersmann, Pathway to cryogen free production of hyperpolarized krypton-83 and xenon-129, PLoS One 7 (2012) e49927.
[49] F. Hill-Casey, T. Hotchkiss, K.A. Hardstone, I. Hitchcock, V. Novak, C.M. Schlepütz, T. Meersmann, G.E. Pavlovskaya, S.P. Rigby, Hyperpolarised xenon MRI and time-resolved X-ray computed tomography studies of structure-transport relationships in hierarchical porous media, Chem. Eng. J. 405 (2021) 126750, https://doi.org/10.1016/j.cej.2020.126750.
[50] G. Pavlovskaya, J. Six, T. Meersman, N. Gopinathan, S.P. Rigby, NMR imaging of low pressure, gas-phase transport in packed beds using hyperpolarized xenon-129, AIChE J. 61 (2015) 4013–4019.
[51] C.Y. Cheng, C.R. Bowers, Direct observation of atoms entering and exiting L-alanyl-L-valine nanotubes by hyperpolarized xenon-129 NMR, J. Am. Chem. Soc. 129 (2007) 13997–14002, https://doi.org/10.1021/ja074563n.
[52] J. Jeener, B.H. Meier, P. Bachmann, R.R. Ernst, Investigation of exchange processes by 2-dimensional NMR-spectroscopy, J. Chem. Phys. 71 (1979) 4546–4553, https://doi.org/10.1063/1.438208.
[53] S. Anala, G.E. Pavlovskaya, P. Pichumani, T.J. Dieken, M.D. Olsen, T. Meersmann, In situ NMR spectroscopy of combustion, J. Am. Chem. Soc. 125 (2003) 13298–13302.
[54] F. Zamberlan, C. Lesbats, N.J. Rogers, J.L. Krupa, G.E. Pavlovskaya, N.R. Thomas, H.M. Faas, T. Meersmann, Molecular sensing with hyperpolarized^{129}Xe using switchable chemical exchange relaxation transfer, Chemphyschem 16 (2015) 2294–2298.
[55] J.H. Gao, L. Lemen, J.H. Xiong, B. Patyal, P.T. Fox, Magnetization and diffusion effects in NMR imaging of hyperpolarized substances, Magn. Reson. Med. 37 (1997) 153–158.
[56] Z.I. Cleveland, T. Meersmann, Binary-collision-induced longitudinal relaxation in gas-phase Kr-83, J. Chem. Phys. 129 (2008) 244304, https://doi.org/10.1063/1.3029663.244304.
[57] J.M. Wild, J.C. Porter, P.L. Molyneaux, P.M. George, I. Stewart, R.J. Allen, R. Aul, J.K. Baillie, S.L. Barratt, P. Beirne, et al., Understanding the burden of interstitial lung disease post-COVID-19: the UK Interstitial Lung Disease-Long COVID Study (UKILD-Long COVID), BMJ Open Respir. Res. 8 (2021) 10, https://doi.org/10.1136/bmjresp-2021-001049.
[58] G.E. Pavlovskaya, T. Meersmann, C.Y. Jin, S.P. Rigby, Fluid flow in a porous medium with transverse permeability discontinuity, Phys. Rev. Fluids 3 (2018), https://doi.org/10.1103/PhysRevFluids.3.044102.
[59] S. Korchak, W. Kilian, L. Schröder, L. Mitschang, Design and comparison of exchange spectroscopy approaches to cryptophane-xenon host-guest kinetics, J. Magn. Reson. 265 (2016) 139–145, https://doi.org/10.1016/j.jmr.2016.02.005.
[60] T. Meersmann, J.W. Logan, R. Simonutti, S. Caldarelli, A. Comotti, P. Sozzani, L. G. Kaiser, A. Pines, Exploring single-file diffusion in one-dimensional nanochannels by laser-polarized Xe-129 NMR spectroscopy, J. Phys. Chem. A 104 (2000) 11665–11670.
[61] K.W. Miller, N.V. Reo, A. Uiterkamp, D.P. Stengle, T.R. Stengle, K.L. Williamson, Xenon NMR - chemical-shifts of a general anesthetic in common solvents, proteins, and membranes, Proc. Natl. Acad. Sci. U.S.A.-Biol. Sci. 78 (1981) 4946–4949, https://doi.org/10.1073/pnas.78.8.4946.
[62] K. Bartik, P. Choquet, A. Constantinesco, G. Duhamel, J. Fraissard, J.N. Hyacinthe, J. Jokisaari, E. Locci, T.J. Lowery, M. Luhmer, et al., Xenon NMR as a probe for microporous and mesoporous solids, Polym., Liq. Cryst., Sol., Flames, Proteins, Imaging, Actual. Chimique (2005) 16–34.
[63] M. Boventi, M. Mauri, K. Golker, J.G. Wiklander, I.A. Nicholls, R. Simonutti, Porosity of molecularly imprinted polymers investigated by NMR spectroscopy, ACS Appl. Polym. Mater. 4 (2022) 8740–8749, https://doi.org/10.1021/acsapm.2c01084.
[64] N.J. Rogers, F. Hill-Casey, K.F. Stupic, J.S. Six, C. Lesbats, S.P. Rigby, J. Fraissard, G.E. Pavlovskaya, T. Meersmann, Molecular hydrogen and catalytic combustion in the production of hyperpolarized Kr-83 and Xe-129 MRI contrast agents, P. Natl. Acad. Sci. U.S.A. 113 (2016) 3164–3168.
[65] J. Eills, D. Budker, S. Cavagnero, E.Y. Chekmenev, S.J. Elliott, S. Jannin, A. Lesage, J. Matysik, T. Meersmann, T. Prisner, et al., Spin hyperpolarization in modern magnetic resonance, Chem. Rev. 123 (2023) 1417–1551, https://doi.org/10.1021/acs.chemrev.2c00534.